SPE-180051-MS

New Insight to Wormhole Formation in Polymer Gel During Water Chasefloods Using Positron Emission Tomography PET

B. Brattekås, The National IOR Centre of Norway, Dept. of Petroleum Technology, University of Stavanger; M. Steinsbø, A. Graue, and M. A. Fernø, Dept. of Physics and Technology, University of Bergen; H. Espedal, Molecular Imaging Center, Dept. of Biomedicine, University of Bergen; R. S. Seright, New Mexico Petroleum Recovery Research Centre

This paper was prepared for presentation at the SPE Bergen One Day Seminar held in Bergen, Norway, 20 April 2016.

Abstract

Polymer gel is frequently used for conformance control in fractured reservoirs, where it is injected to reside in fractures or high-permeability streaks to reduce conductivity. With successful polymer gel conformance control in place, increased pressure gradients across matrix blocks may be achieved during chasefloods, diverting water, gas or EOR chemicals into the matrix to displace oil. Knowledge of gel behavior during placement and chase floods is important, because it largely controls the success of subsequent injections. Polymer gel behavior is often studied in core floods, where differential pressure and effluents from fracture and matrix outlets give information about gel deposition during placement and flow paths during chasefloods. The work presented in this paper utilize complimentary PET-CT imaging to quantify the behavior and blocking capacity of Cr(III)-Acetate HPAM gel during chase waterflooding. *In-situ* imaging provides information about changes that may not be extracted from pressure measurements and material balance only, such as changes in local fluid saturations and dynamic spatial flow within the fracture and within the structure of the gel network.

Polymer gel was placed in core plugs with longitudinal fractures that connected the inlet and outelt, and chase water was subsequently injected to measure the gel blocking capacity. The water phase was labelled with a positron emitting radiopharmaceutical (F-18) to visualize and quantify local flows with positron emission tomography (PET) during gel rupture and subsequent flooding. Using PET, we study gel rupture and the development of wormholes during gel erosion after rupture as a function of flow rate. A particular strength with access to dynamic, local flow patterns is the direct comparison to global measurements, such as differential pressure and production rate, to verify existing gel behavior models.

Introduction

Channeling of injected fluids through a high permeable fracture network, and the following early fluid breakthrough, may be mitigated by placing a highly viscous polymer gel in the fracture [1–3]. With polymer gel in place, higher differential pressures may be achieved during chasefloods and contribute to increased sweep efficiency in the porous matrix adjacent to the fracture network. Gel placement in fractures and gel blocking capacity during chasefloods has been thoroughly investigated and discussed in the literature; see e.g. [4–6]. A polymer gel is formed when a gelant solution (a mixture containing all chemical components to form a polymer gel) is exposed to elevated temperature for a given time known as the gelation time. Previous work investigated how the gel state during placement (gel or gelant) influenced the gel behavior during chasefloods [4]. In this work we study the extrusion of formed polymer gel through fractures, and its resistance to pressure during subsequent waterfloods.

Formed gel is highly viscous and its structure prevents it from entering significantly into the porous matrix next to the fracture during placement. The gel solvent (water in most cases) may, however, leave the gel during propagation through the fracture and progress into the matrix in a leakoff process. During water leakoff, a *filter cake* of concentrated gel forms in the fracture. The concentrated gel is more rigid compared to the injected gel, and is more pressure resistant. The rate of water leakoff has implications for the rate of gel propagation into a fractured reservoir, as well as the rate of fracture growth during hydraulic fracturing, and was previously investigated by Carter [7–9] and Seright [10–12]. Carter proposed a model for fluid leakoff during hydraulic fracturing, where an important assumption was that the thickness of the filter cake on the fracture faces was uniform at any given time. Seright [10] presented an alternative model for leakoff, suggesting that the filter cake on the fracture wall was aerially and volumetrically heterogeneous, and formed when fragments of injected gel dehydrated and became immobile in the vicinity of where the dehydration occurred. Mobile gel of the original composition flowed through the concentrated gel to advance to the gel front within narrow flow channels, termed *wormholes*. The two proposed leakoff models were similar in terms of leakoff rate, however; the filter cake formation within the fracture was suggested to take place in widely different manners and is an important distinction that strongly influence fluid flow during chasefloods. Figure 1 illustrates filter cake formation during, and due to, water leakoff for the two models: the Carter model on the left, with the filter cake forming on the fracture surfaces only, and the Seright model on the right, with a randomly distributed filter cake forming in the fracture volume.

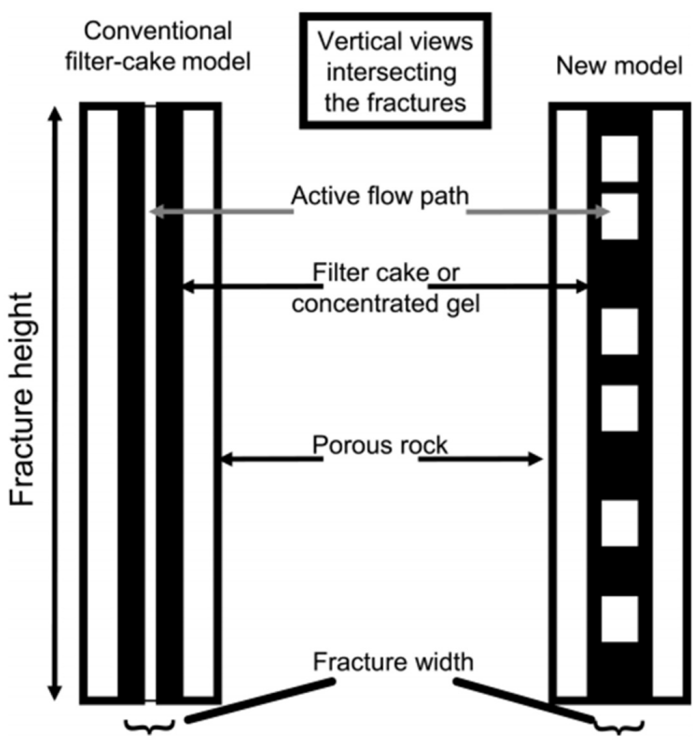

Figure 1—Seright [10] illustrated filter cake formation in each of the two leakoff models: Left: leakoff model by Carter, and Right: leakoff model by Seright. The view is into the cross-section of an open fracture.

Brattekås *et al*. [4] showed, using pressure measurements, that gel resistance during waterflooding was higher in cores after formed gel placement compared to gelant placement with following *in-situ* crosslinking. This was explained by the gel's ability to form wormholes through a filter cake during placement: formed gel dehydrates during propagation through a fracture, which increases its pressure resistance, and fresh gel flows through the concentrated gel in wormholes. During chase waterflooding, fresh gel is displaced from the wormholes at the rupture pressure, and water follows these narrow flow paths through the fracture volume. As long as the injected water is contained in wormholes, fracture permeability remains significantly decreased. During placement of gel in its immature form (as a gelant), and according to the Carter filter cake model for formed gel placement, wormholes do not form. Consequently, gel erosion during waterflooding occurs in a different manner, and may open larger sections of the fracture to flow. Seright [10] injected dyed gel to follow gel of the same composition (not dyed) into a fracture, and could thus visualize the formation of wormholes during gel injection. After chase waterflooding, wormhole patterns can be clearly visible when opening the used core and inspecting the fracture surfaces [4, 13]. The development of wormholes during dynamic chase waterfloods have, however, only been investigated through global measurements of pressure and flow rate. In this study, we used positron emission tomography (PET) to identify this phenomenon *in-situ*. PET imaging is based on the decay of positron-emitting radionuclides. The positron loses kinetic energy by interactions with the surroundings, and at near-zero momentum the positron is emitted from the nucleus accompanied by an electron to balance atomic charge. Radioactivity is a spontaneous nuclear phenomenon, that is insensitive to temperature and pressure [14]. PET was recently used to study flow in tight rock samples, and the results were compared with CT imaging [15]. In this work, PET was used to visualize flow of radioactive water through a gel-filled fracture, to augment global measurements, and to increase the understanding of filter cake formation during formed gel placement and wormhole formation during chasefloods.

Experimental section

Experimental Schedule

The experimental schedule consisted of three steps: 1) core plug preparation, 2) polymer gel placement, and 3) chase waterflooding to measure gel blocking capacity and investigate the development of wormholes. *In-situ* imaging by positron emission tomography (PET) was used during step 3, to visualize and quantify the flow of water through a gel-filled fracture.

Core Plug Preparation Highly heterogeneous outcrop limestone from the Edwards formation in Texas, USA, with trimodal pore sizes, vugs and microporosity [16, 17], and homogeneous sandstone [1] from the Gildenhausen quarry in Bentheimer, Germany [18, 19] was used to study chaseflood behavior through gel-filled fractures. Cylindrical core plugs with 4.96cm diameter were drilled from larger outcrop limestone and sandstone blocks and cut to length ($L_{limestone}$ = 7.56cm and $L_{sandstone}$ = 10.12cm). Smooth, longitudinal fractures were created through the cores using a band saw, and the core surfaces were gently washed using tap water to remove lose grains. The core fragments were dried at an elevated temperature of 60^{o}C for one week. Fractured cores were assembled using clamps and POM (polyoxymethylene) spacers to maintain a constant fracture aperture of 1mm. Surfaces were covered in epoxy resin, and only the fracture surfaces were left open to flow. POM end pieces were designed, featuring three inlets and three outlets, separating the fracture from each matrix core half. The end pieces were glued to the core inlet and outlet end faces using epoxy resin. After drying, holes were drilled through the epoxy into the matrix core halves to allow flow. The assembled cores were covered in several layers of epoxy resin to increase the resistance to flow, and could thus be used in flooding experiments with no additional

[1] The results for the sandstone core plug are previously published in 4. Brattekås, B., et al., *Washout of Cr(III)-Acetate- HPAM Gels From Fractures: Effect of Gel State During Placement*. SPE Production & Operations, 2015. 30(02): p. 99–109.

overburden pressure. The core plugs were saturated with brine (4wt% NaCl, 3.4wt% $MgCl_2*6H_2O$, 0.5wt% $CaCl_2*2H_2O$) after assembly and porosity calculated from weight measurements.

Polymer gel placement 0.5% HPAM polymer (~5 million Daltons molecular weight) and 0.0417wt% Cr(III)-acetate was mixed in brine (4wt% NaCl, 3.4wt% $MgCl_2*6H_2O$, 0.5wt% $CaCl_2*2H_2O$) to form gelant. After thorough mixing, the gelant solution was placed in a stainless steel accumulator and aged at 41°C for 24 hours (five times the gelation time) to form mature polymer gel. The gel was allowed to cool to ambient conditions (approximately 23°C) before injection into the fractured core plugs, using injection rates of 200mL/h (limestone) and 6mL/h (sandstone). Leakoff was recorded by volumetric measurements of brine effluent exiting the matrix outlets as a function of time. After gel placement, the cores were shut-in for 24 hours with all inlets and outlets closed.

Water chasefloods Water chasefloods were performed to measure the blocking capacity of the gel present in the fractures. We used high salinity brine, with the same composition as the gel solvent. A schematic of the experimental setup for gel placement and chase waterflooding may be viewed in Figure 2.

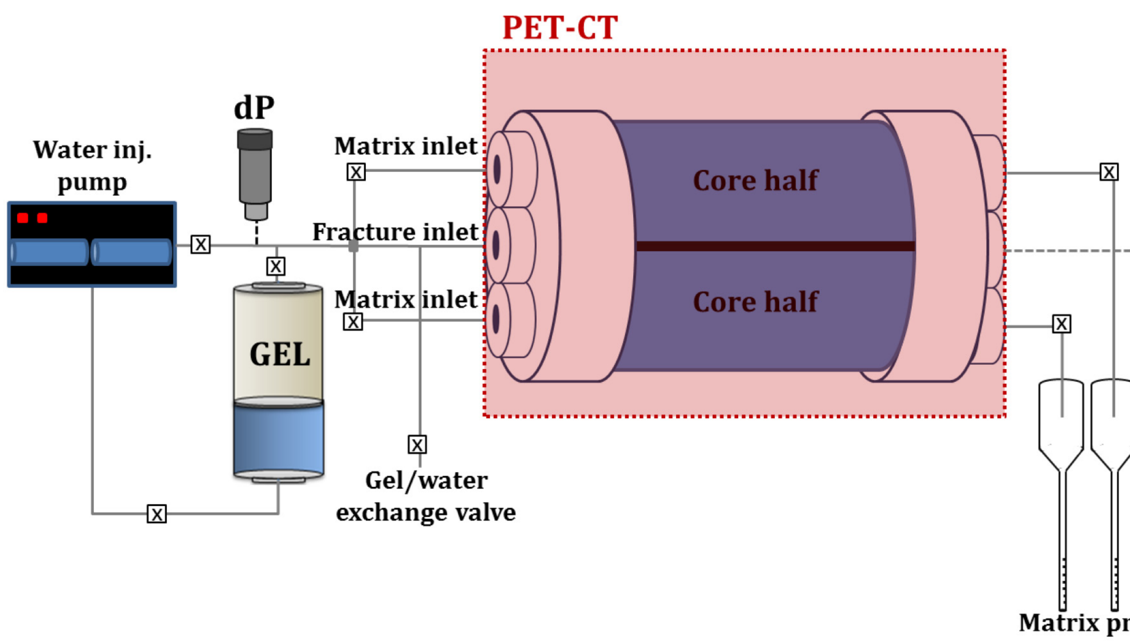

Figure 2—Schematic of the experimental setup for gel placement and chase waterflooding. Pressure and volumetric measurements or *in-situ* imaging by PET were used to quantify gel behavior.

The water injection rate was initially low at 6mL/h to accurately measure the *rupture pressure* (the pressure at which the gel in the fracture breaks and allows fluids to flow through it). When the differential pressure across the fracture stabilized after gel rupture, eight sequential waterflood cycles were performed in the sandstone core: the water flow rate was first increased stepwise from 6 - 60 - 300 - 600mL/h (termed an increasing rate cycle) and thereafter reduced in the same manner (termed a decreasing rate cycle). The limestone core was imaged in the PET-scanner during waterflooding, to visualize and quantify the flow of water through the gel-filled fracture. Two sequential waterflood cycles were performed, where the water flow rate was first increased from 6 - 60 - 300mL/h, and thereafter stepwise decreased. The waterflood was thereafter left at the lowest rate (6mL//h) for thirteen hours. The pressure across the fracture was measured as a function of time and flow rate during waterflooding for both cores, and the results from global measurements were compared to *in-situ* imaging.

Positron Emission Tomography (PET) imaging

A small-animal PET-CT scanner was used for *in-situ* imaging during chase waterflooding in the limestone core plug. Fack *et al*. [20] and Haldorsen *et al*. [21] used the same PET-CT for pre-clinical studies in rats and mice, and the experimental procedure for PET imaging was adapted for use in core plugs: ^{18}F was produced by a local cyclotron and used to synthesize ^{18}F-fluorodeoxyglucose (^{18}F-FDG), which is a water-soluble fluorine radioisotope with a half-life of $t_{1/2}=109$ minutes. Spatial fluid saturations in the core plug and fracture were calculated based on the registered activity of the labeled brine phase at given time steps. PET/CT sequences were acquired on a CT 80 W Nanoscan PC imager, featuring spatial resolutions of 800p,m and 30p,m of the respective PET- and CT detector systems [21]. The PET field of view (FOV) was 9.5 × 8cm in axial and trans-axial directions, allowing imaging of the entire core plug and most of the end pieces. The PET detectors consist of LYSO crystals, and acquisition was performed in 1:5 coincidence and normal count mode. A CT scan (helical projections with tube energy of 70kvP, exposure time 300ms, 720 projections, max FOV, binning 1:4) was acquired for core plug positioning; the tube voltage was, however, not high enough to correctly reproduce the spatial core plug density and attenuation correction from CT during PET data reconstruction was therefore not applied. During initial waterflooding ^{18}F-FDG was mixed in 300mL brine at 151MBq activity and PET was acquired for two hours during stepwise alteration of the water injection rate. After 12 hours of continuous waterflooding, ^{18}F-FDG at 183MBq activity was mixed in a new batch of brine (300mL) and injected into the fracture. PET was acquired for one hour during continued low rate waterflooding.

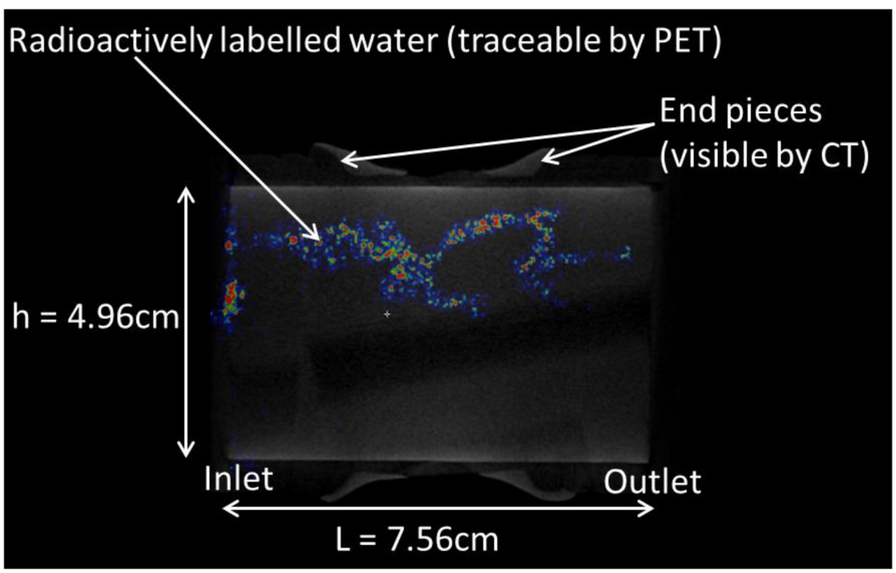

Figure 3—View inside the longitudinal, vertically aligned fracture of the limestone core plug placed in the PET-CT scanner. The grey outline is the CT image of the core (used for positioning). Bedding planes in the rock surface may be observed as darker features, and were constant in all images. The colored signal is water labelled with ^{18}F-FDG, and recorded by Positron Emission Tomography (PET).

Results and Discussion

Polymer gel placement

The rate of water leakoff during gel propagation through open fractures was measured in several previous publications [4, 10] and shown to be: 1) independent of core material (for fully water saturated core plugs), and 2) largely independent of the gel injection rate. Seright [10] found that, when using short fractures, *screen-out* of gel (where concentrated gel is flushed out of the fracture due to turbulent flow) could occur at high gel flow rates (>2000mL/h). In this study, lower, constant injection rates of 200mL/h (for the limestone) and 6mL/h (for the sandstone) were used. The limestone core (porosity,0= 22.9%, permeability, K=13mD [22]) was mounted in the PET scanner during gel injection, and volumetric measurements for leakoff calculation were not performed. The leakoff rate measured during gel injection into the sandstone core (0=23% and K=1.2D) was lower than expected from the leakoff models (Figure 4, left). The measured differential pressure across the fractures during gel injection is shown in Figure 4, right.

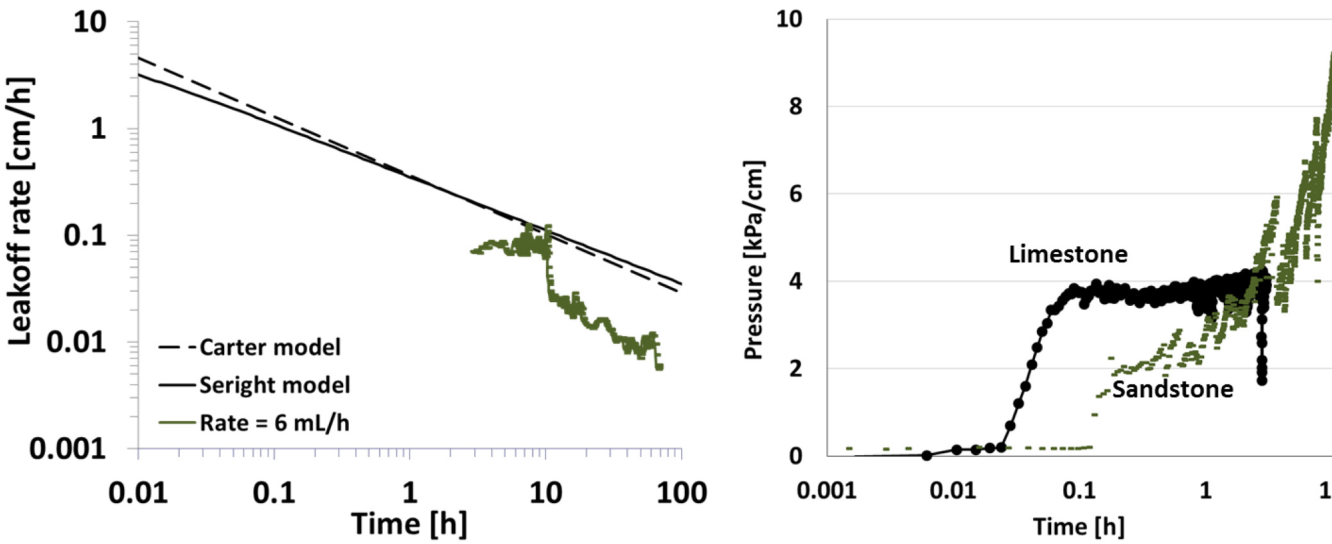

Figure 4—Left: Measured leakoff rate for the sandstone core. Right: differential pressure during gel injection at 200mL/h and 6mL/h into the fractured core plugs.

Water chasefloods

Calculations based on global measurements Waterflooding was performed to measure the gel blocking capacity and analyze the development of wormholes through the gel-filled fractures. The differential pressure across the fractures was logged during waterfloods for the two core plugs and formed, together with rate data, the basis for calculations and comparisons in this section.

Rupture pressures were 4.5kPa/cm and 4.4kPa/cm for the sandstone and limestone core, respectively, and corresponded well with previously reported rupture pressure data after formed gel placement in fractures [4, 13]. When the gel ruptures, water may again flow through the fracture by following the rupture path (according to the Seright leakoff model the rupture path will be the randomly distributed wormholes through concentrated gel); measuring the pressure drop and flow rate during chase waterfloods through gel-filled fractures gives an estimate of gel behavior. In the sandstone core, eight increasing and decreasing rate cycles were performed, whereas two cycles were performed in the limestone core. The pressure gradients measured during water injection at the specific rate steps (6 mL/h, 60 mL/h, 300mL/h and 600mL/h) are shown in Figure 5 as functions of the effective brine velocity through the fracture. The measurements were taken for each rate step when the pressure response across the gel-filled fracture had stabilized at a close-to-constant value. Figure 5 (left) shows the initial rupture pressure and the following pressure response during the first two increasing/decreasing rate cycles in both core plugs. The rupture pressures are denoted by a red dot (limestone) and a black triangle (sandstone) in the figure. The gel behavior during water chaseflooding was similar in the two core plugs: after gel rupture, water could pass through the fracture and the pressure gradient across the fracture decreased for the lowest water flow rate. When the flow rate was increased to 60mL/h, the measured pressure gradient across the fracture continued to decrease, probably caused by further erosion of gel around the wormholes formed in the fracture. Increasing the flow rate further, to 300mL/h and 600mL/h, yielded an increase in the measured pressure gradient up to the initial post-rupture level. When the flow rate was stepwise decreased back towards

6mL/h, significantly lower pressure gradients were measured for each specific rate. This was expected behavior, attributed to erosion of gel in the wormholes during water injection.

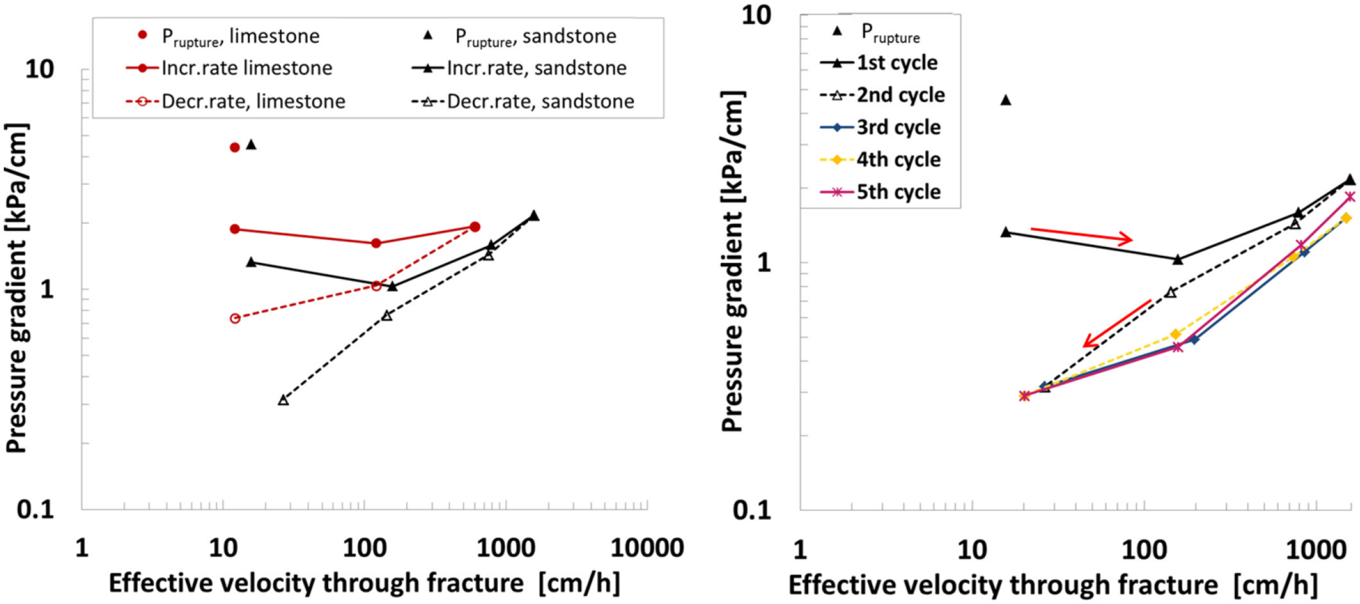

Figure 5—Measured pressure gradients as functions of the effective velocity of brine through the fractures. Left: the limestone core (red curves) and the sandstone core (black curves) during the first two increasing and decreasing rate cycles. The dotted lines represent decreasing rate cycles and the solid-drawn lines represent cycles where the injection rate increases. Right: The first five increasing/decreasing rate cycles, out of eight in total, for the sandstone core.

With the water flow rate back at the initial level (6mL/h), two different waterflood schedules were performed in the core plugs: in the limestone core, low rate waterflooding was continued for 13 hours, while six additional decreasing/increasing injection rate cycles were performed in the sandstone core. Figure 5 (right) shows the first five increasing/decreasing rate cycles in the sandstone core, out of eight cycles in total. The pressure gradients for each specific rate continued to decrease during the third cycle (increasing rate), with respect to the first two cycles. From the third cycle, however, the pressure gradients remained on the same level within each flow rate, suggesting a stable system with minor gel erosion, although more than 120 fracture volumes (FV) of water had passed through the fracture at this point. The elasticity of the gel enabled it to maintain a stable and high pressure resistance after rupture and significant water throughput, because wormholes are allowed to collapse and re-open during waterflooding depending on the water flow rate.

Wormhole widths for the two cores could be calculated from the measured differential pressure and rate data. The wormhole width is in the following defined as the effective channel width open to flow (after gel rupture), and was calculated by Poisseuille's law, using the following assumptions:

1. Fluid flow will only occur through the wormholes and not through the concentrated gel in the fracture.
2. For the purpose of this calculation, there is only one wormhole present in the fracture.
3. The wormhole is assumed to be of cylindrical shape, thus the calculation is only valid for as long as the wormhole width (the diameter of the cylinder) is less than the fracture aperture.

Figure 6 (left) shows the wormhole width as a function of water throughput for the sandstone core plug. The wormhole width increased with increasing injection rates. A spread within each specific rate was also observed; initially, the wormhole width increased with water throughput, due to gel erosion, and thereafter stabilized at a close to constant value for each given rate. The wormhole width stabilized after the third waterflood cycle, and was on average calculated to be 0.022cm (6mL/h), 0.036cm (60mL/h), 0.043cm (300mL/h) and 0.045cm (600mL/h). Figure 6 (right) shows the calculated wormhole width for the limestone core plug (black squares) and compares the data to the results for the sandstone core plug. Wormhole development was similar in the gel-filled fractures of the two core plugs, indicating that gel behavior visualized and quantified by PET in the next section (for the limestone core only) is representative for waterflooding after formed gel placement in an open fracture. Two waterflood cycles were performed in the limestone core, and the stepwise adjustments in rate continued for 2 hours of water injection: at this time, the system was not fully stabilized and further gel erosion may be expected to occur. The calculated wormhole widths were 0.018cm (6mL/h), 0.029cm (60mL/h) and 0.037cm (300mL/h) for the limestone core, which corresponds well with the sandstone core, considering a lower degree of gel erosion. During continued low rate waterflooding, the differential pressure across the fracture was slowly decreasing, indicating further gel erosion. After significant water throughput (13 hours and >40FV), the wormhole width was calculated to be 0.048cm and comparable to the wormhole width at the highest degree of gel erosion in the sandstone core.

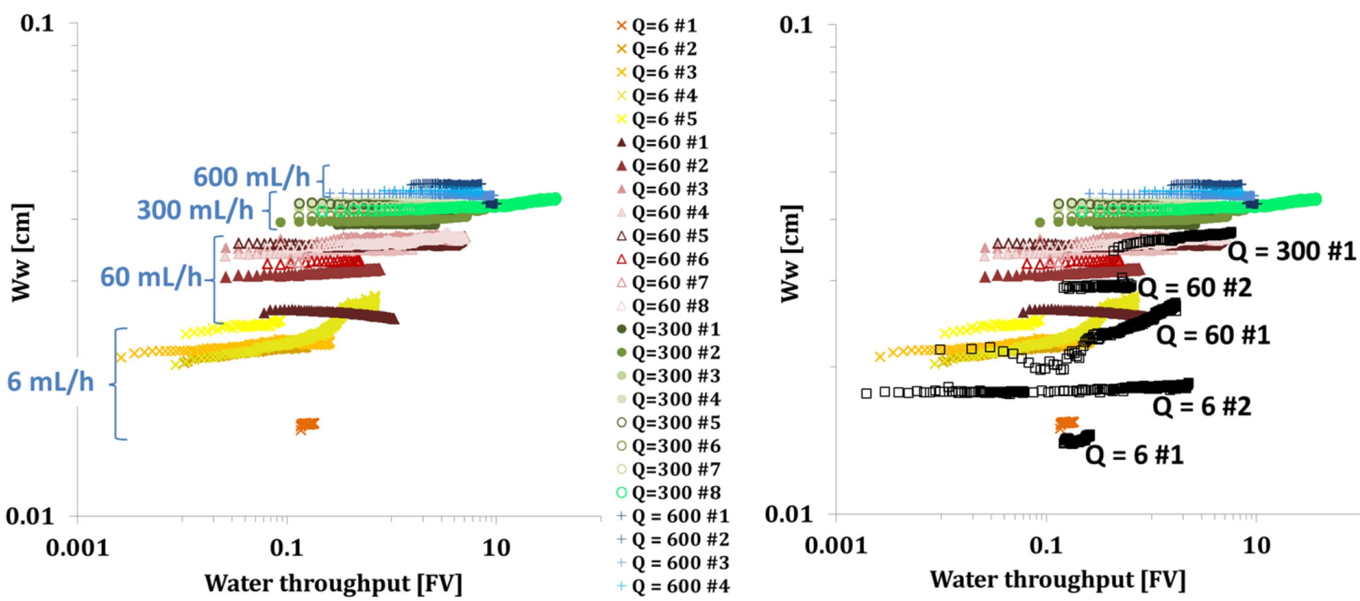

Figure 6—Wormhole widths based on calculations from global measurements. Left: Wormhole width (y-axis) as a function of water throughput at each specific rate for the sandstone core. The wormholes increase in size with injection rate, and for each injection rate the wormhole width initially increases with the flow of water through the fracture. After several waterflood cycles the wormholes stabilize due to minor gel erosion. Right: the black squares show the calculated wormhole widths for the limestone core, compared to the sandstone core. Q denotes the specific rate for each curve.

In-situ investigations of wormhole development using Positron Emission Tomography (PET) PET imaging was used to investigate water flow through a gel-filled fracture *in-situ*. Injection brine was labelled by ^{18}F-FDG prior to waterflooding; it was therefore possible to visualize and quantify the spatial saturation of water through the fracture by PET, as a function of flow rate and time. To closely investigate the water flow pattern during the increasing and decreasing rate cycles, six images were constructed from the PET-data- one for each rate step. The images were constructed by extracting the PET signal for each rate when the pressure drop across the core was constant and assuming a constant wormhole structure. Figure 7 shows the wormhole flow patterns at different rate stages during the waterflood; view is within the longitudinal fracture.

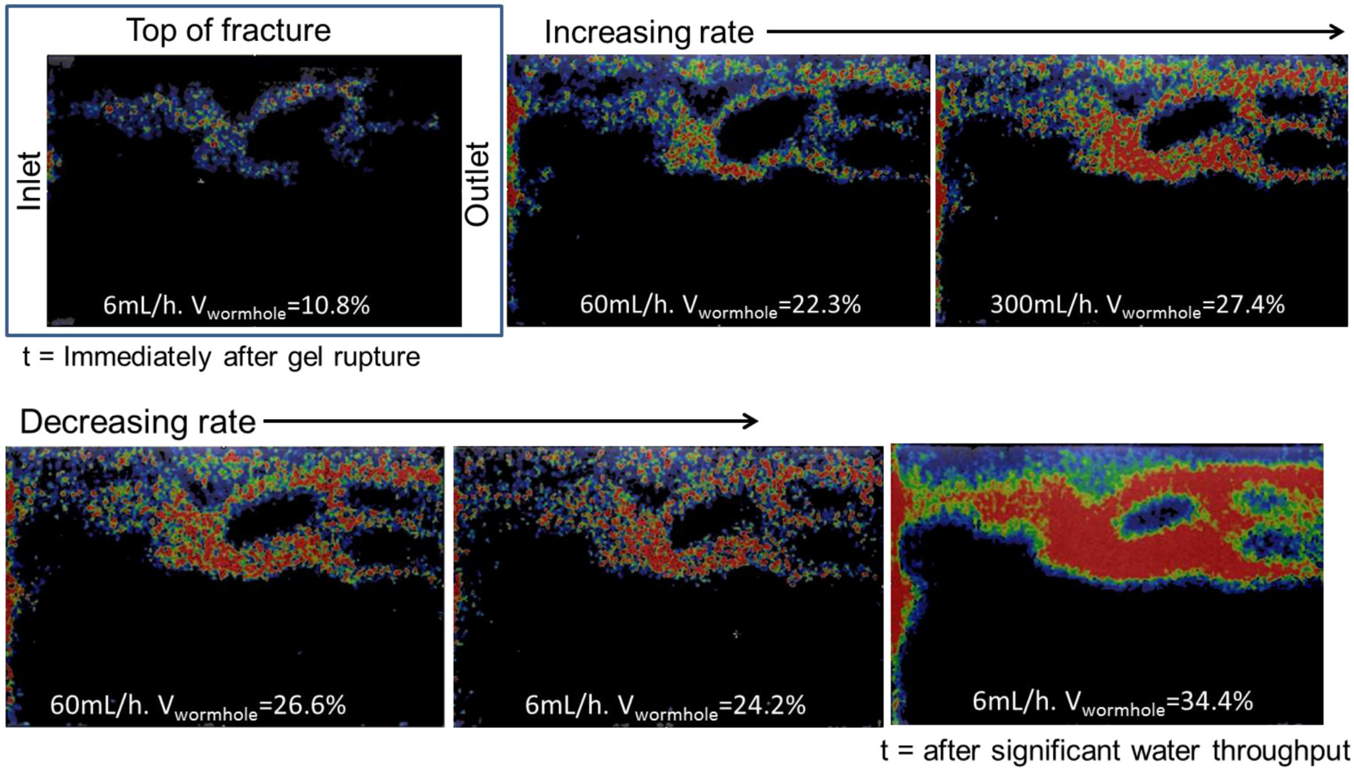

Figure 7—PET images showing the formation of wormholes during chase waterflooding. The colored signal is water traced with radioactive pharmaceutical ^{18}F-FDG. The fracture was vertically aligned, and the top of the images correspond to the top of the fracture. The first image (top, left) shows the wormhole flow path immediately after gel rupture at 6mL/h. The next two rate increases were 60mL/h (top, middle) and 300mL/h (top, right), during which the wormhole flow pattern was extended. Stepwise decreasing the rate to 60mL/h (bottom, left) and 6mL/h (bottom, middle) did not change the flow pattern back to one single conduit. The wormhole flow pattern after significant water throughput (bottom, right) was extended due to gel erosion.

Wormholes and wormhole development with flow rate was clearly seen on the PET images. Figure 7 shows the wormhole formed during initial waterflooding at 6mL/h (left image, top row). The wormhole mostly consists of a single flow conduit at this point, although large scale variations in the size of the rupture path were observed within the fracture volume. 11% of the fracture volume emitted a radioactive signal, i.e. conducted flow of radioactive water, and thus contained wormhole(s). The rest of the fracture was filled with concentrated gel that did not exhibit a signal detectable by PET. When the rate was increased to 60mL/h (Figure 7, center image, top row), the wormhole branched out and filled larger portions of the fracture. New rupture paths were formed through the concentrated gel filter cake compared to the first rate step, and fluid flow was observed through several wormholes spanning between the inlet and outlet. 22% of the fracture volume conducted water flow at 60mL/h, efficiently doubling the wormhole volume since gel rupture. The part of the fracture volume conducting flow of radioactive water (i.e. the wormhole volume) increased further (27%) when the injection rate was increased to 300mL/h (Figure 7, right image, top row), although at a much lower scale. New wormhole flow paths were not created during this rate step, indicating that the increased wormhole volume was caused by erosion of gel around existing wormholes. Figure 7 (lower row) shows the decreasing rate cycle. A reduction in the rate to 60mL/h did not cause a corresponding reduction in the measured wormhole volume, and the wormhole remained in the same shape and location as in the previous rate step. Reducing the flow rate to 6mL/h reduced the wormhole volume to 24% of the fracture volume, without changing the wormhole morphology. Figure 7 (right image, lower row) shows the wormhole flow path after significant water throughput at 6mL/h, where wormholes covered 34% of the fracture volume.

In-situ imaging supported the existence of a non-uniform gel filter cake in the fracture, and we observed that (for the first two waterflood cycles) 1) the wormholes are in the same location from the initial breach to late waterflooding, 2) the wormholes are, for the most part, in the same shape for the duration of waterflooding, although new rupture paths were added to the original rupture path when the flow rate was increased above the original level, 3) the wormholes are eroded wider when higher and higher rates are used, 4) but the wormholes do not collapse when the rate is lowered, and 5) extended waterflooding substantially erodes gel along the fracture-width direction but does not form new wormhole pathways.

Wormhole development: in-situ measurements compared to global calculations We converted the total measured wormhole volume in the fracture, given in the previous section, to average wormhole widths using simple calculations of geometry: we assumed that the wormhole had a rectangular shape, where one side was fixed at the fracture aperture and the other side was the wormhole width (Ww) (not fixed). The wormhole was thus envisioned to expand and retract vertically within the fracture volume (i.e., in the largest dimension of the fracture). *In-situ* imaging by PET (e.g. Figure 7) showed large variations in the wormhole width, from very narrow (almost invisible on images) in some sections of the fracture to spanning almost half the fracture height in other sections. The uncertainty contained in an average value for the wormhole width is therefore large, however; it was necessary to use these values to compare *in-situ* imaging to calculations from global measurements. Measured and calculated wormhole widths are compared and shown in Figure 8. Measured average wormhole widths were more than thirty times higher than the calculated values for each specific rate, and do not account for the high pressure gradients achieved during post-rupture waterflooding. This indicates that the average wormhole width is not a good measure for the actual conductivity of the fracture, and is not the controlling factor for flow. The difference in wormhole morphology is an important distinction between calculations and measurements that may explain this deviation: a single, uniform wormhole spanning from the fracture inlet to the fracture outlet was assumed to be the only conductor for flow in the calculations from global measurements. *In-situ* imaging by PET revealed the existence of several wormholes, seemingly randomly distributed within the fracture volume, and with significant variations in width. Image analysis software ImageJ identified the smallest wormhole width (where the signal was barely visible on the images) to be 0.001cm, which was less than all calculated values from global measurements. Narrow constrictions in the wormhole flow paths will act as natural chokes on fluid production and control the pressure response across the fracture during subsequent floods. This mechanism is only possible when the filter cake forming in the fracture during gel placement is heterogeneous, thus the paths of gel rupture during subsequent floods (presumably in wormholes) are naturally non-uniform and dependent on local gel concentration.

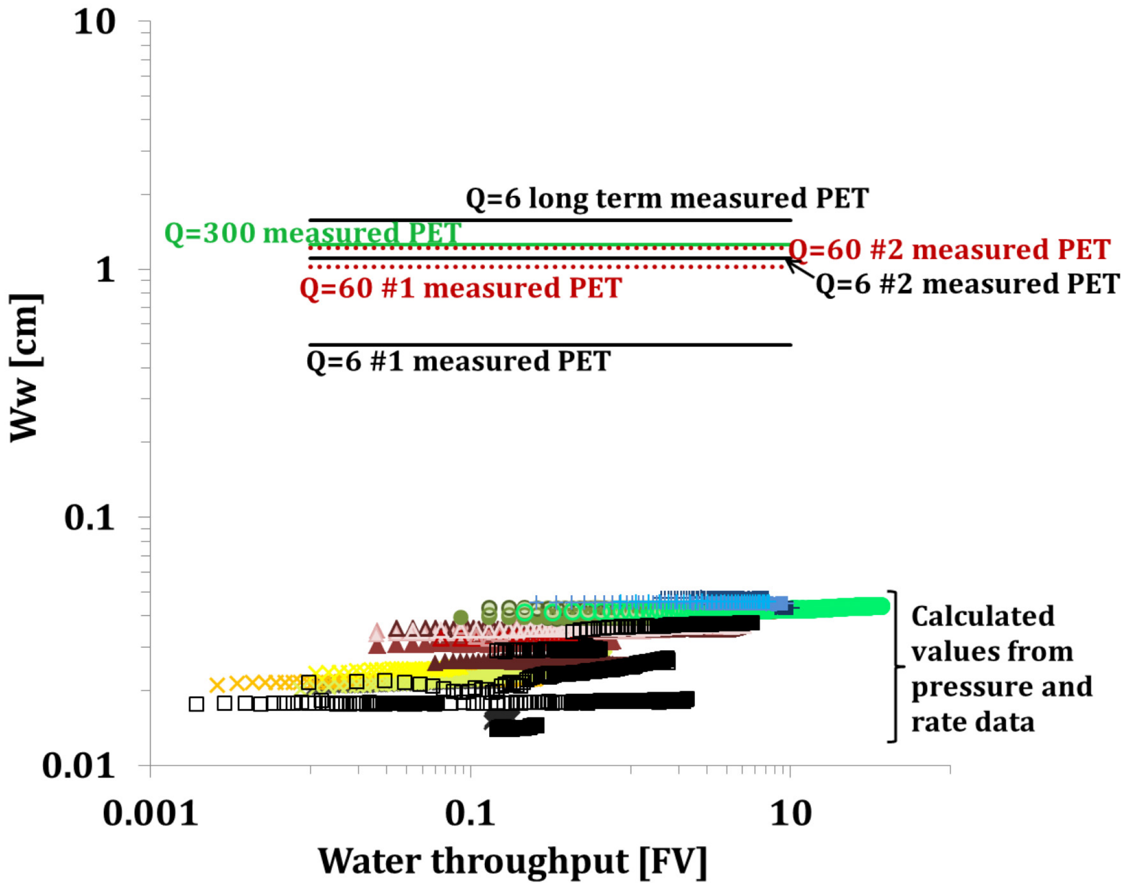

Figure 8—Calculated wormhole width from pressure measurements compared to measured wormhole width from *in-situ* imaging by PET.

Average gel concentration varies with lengthwise position in a fracture, with higher concentrations close to the fracture inlet and a decreasing concentration towards the fracture outlet. For the limestone core, a clear relationship between fracture position and wormhole width was not found, possibly due to the use of a short fracture. For all rate steps, the narrow flow paths were found close to the fracture inlet and outlet, and the largest wormhole widths were measured in the second and third quarters of the fracture length.

Advantages of in-situ imaging Several previous publications have supported the existence of a non-uniform gel filter cake in the fracture after formed gel placement: Seright [10] injected dyed gel to follow gel of the same composition (not dyed) into a fracture, and observed that gel of injected composition flowed through concentrated gel in wormholes during gel placement, shown in Figure 9 (left). Brattekås *et al*. [4] and Brattekås *et al*. [13] observed clearly visible wormhole patterns resulting from chase waterfloods when gel-filled fractures were opened and fracture surfaces inspected after chase waterflooding (Figure 9, center). The development of wormholes during dynamic chase waterfloods was investigated by positron emission tomography (PET) in this study (Figure 9, right) with clear advantages: *In-situ* imaging by PET only relied on the presence and decay of radioactive water in the core, and could be performed during dynamic floods for several different flow rates and time steps. PET is able to catch and quantify quick changes in polymer gel networks during chase waterfloods without damaging the core or gel, thus the core can be used further in experiments. Visual inspection of fracture surfaces, as in Figure 9 (middle), requires the core to be broken apart, and the core cannot be used further, e.g. to investigate and compare EOR chasefloods to already performed water chasefloods. In addition, the observations made are highly qualitative, and dynamic changes resulting from differences in pressure and rate are not captured. *In-situ* imaging by PET will be used in future work to augment previous experiments on e.g. the effect of gel state during placement [4], and the mechanism behind low-salinity waterfloods for improved high- salinity gel blocking [13].

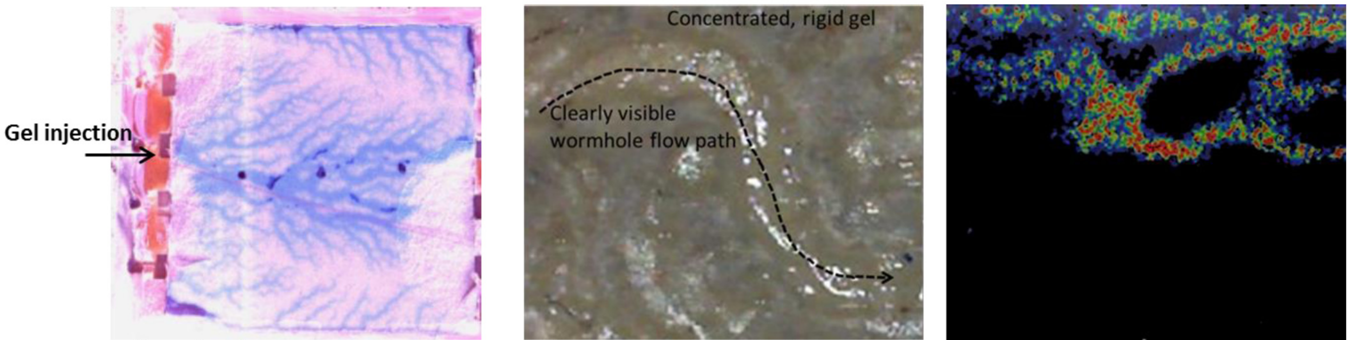

Core broken apart after gel injection where dyed gel followed non-dyed gel

Core broken apart after waterflooding to reveal worm-holes

In-situ visualization by PET for dynamic quantification of wormhole morphology

Figure 9—Left: Dyed gel injection following gel of the same composition (not dyed) from Seright [10]. Center: clearly visible wormhole after waterflooding from Brattekås *et al*. [13]. Right: PET imaging of a complete wormhole flow pattern in a gel-filled fracture still intact.

Conclusions

- *In-situ* imaging by positron emission tomography (PET) is a good and efficient method for investigating water chasefloods through gel-filled fractures.
- We used PET to investigate the development of wormholes during dynamic waterfloods. PET imaging supported the existence of a non-uniform gel filter cake in the fracture.
- The wormhole width, measured by PET, varied significantly within the fracture volume, and did not correspond to calculated values from pressure and rate data.
- The average wormhole width measured by PET is not a good indication of fracture flow capacity. Fracture flow and pressure response across the fracture is controlled by narrow constrictions in the wormhole flow path.
- Wormholes covered 11% of the fracture volume immediately after gel rupture, visualized by PET.
- New rupture paths (wormholes) were added to the original gel rupture path when the water flow rate was increased above the initial level.
- After the wormhole(s) had expanded, they remained in the same shape and location for the entire waterflood, and changes in the wormhole volume with rate was attributed to gel erosion (during increasing rate cycles) and gel elasticity (wormholes collapsing during decreasing rate cycles).
- Wormhole collapse was not significant during the two increasing/decreasing rate cycles performed in the limestone core.
- Extended waterflooding was observed to substantially erode the gel along the fracture-width direction, however, without forming new wormhole pathways.
- The high initial pressure response of the gel was not restored after rupture and significant water throughput. A high pressure level was, however, maintained for the sandstone core during several increasing/decreasing rate cycles when gel erosion had stabilized after three consecutive rate cycles.

Acknowledgements

The PET-CT scanner was used in collaboration with the Molecular Imaging Centre (MIC), Department of Biomedicine, UiB, Norway. The authors wish to acknowledge senior engineer Cecilie Brekke Rygh for training.

The authors acknowledge the Research Council of Norway and the industry partners; ConocoPhillips Skandinavia AS, BP Norge AS, Det Norske Oljeselskap AS, Eni Norge AS, Maersk Oil Norway AS, DONG Energy A/S, Denmark, Statoil Petroleum AS, GDF SUEZ E&P NORGE AS, Lundin Norway AS, Halliburton AS, Schlumberger Norge AS, Wintershall Norge AS of The National IOR Centre of Norway for support.

References

1. Portwood, J. T. Lessons Learned from Over 300 Producing Well Water Shut-Off Gel Treatments. in SPEMid-Continent Operations Symposium. 1999. Oklahoma City, OK, USA.
2. Willhite, G. P. and R. E. Pancake, Controlling Water Production Using Gelled Polymer Systems. *SPE Reservoir Evaluation & Engineering,* 2008. **11**(3): p. 454–465.
3. Seright, R. S., R. H. Lane, and R. D. Sydansk, A Strategy for Attacking Excess Water Production. *SPE Production and Facilities,* 2003. **18**(03): p. 158–169.
4. Brattekås, B., et al., Washout of Cr(III)-Acetate-HPAM Gels From Fractures: Effect of Gel State During Placement. *SPE Production & Operations,* 2015. **30**(02): p. 99–109.
5. Seright, R. S., Washout of Cr(III)-Acetate-HPAM Gels from Fractures, in International Symposium on Oilfield Chemistry. 2003, Society of Petroleum Engineers: Houston, TX
6. Ganguly, S., et al., The Effect of Fluid Leakoff on Gel Placement and Gel Stability in Fractures. *SPE Journal,* 2002. **7**(03): p. 309–315.
7. Penny, G. S. and M. W. Conway, ″Fluid Leakoff’, Recent Advances in Hydraulic Fracturing. *Monograph Series,* ed. J. L. Gidley. Vol. **12**. 1989, Richardson, Texas: SPE.
8. Howard, G. C. and C. R. Fast, Hydraulic Fracturing. *Monograph series*. Vol. **2**. 1970, Richardson, Texas: SPE.
9. Howard, G. C. and C. R. Fast, Optimum Fluid Characteristics for Fracture Extension. Drilling and Production Practices, 1957. API(261).
10. Seright, R. S., An Alternative View of Filter-Cake Formation in Fractures Inspired by Cr(III)- Acetate-HPAM Gel Extrusion *SPE Production & Facilities,* 2003. **18**(1): p. 65–72.
11. Seright, R. S., Gel Propagation Through Fractures *SPE Production & Facilities,* 2001. **16**(4): p. 225–231.
12. Seright, R. S., Polymer Gel Dehydration During Extrusion Through Fractures. *SPE Production & Facilities,* 1999. **14**(2): p. 110–116.
13. Brattekås, B., A. Graue, and R. S. Seright, Low-Salinity Chase Waterfloods Improve Performance of Cr(III)-Acetate Hydrolyzed Polyacrylamide Gel in Fractured Cores. Spe Reservoir Engineering, 2015. In press.
14. Ersland, G., et al., Complementary imaging of oil recovery mechanisms in fractured reservoirs. *Chemical Engineering Journal,* 2010. **158**: p. 32–38.
15. Fernø, M. A., et al., Combined positron emission tomography and computed tomography to visualize and quantify fluid flow in sedimentary rocks. *Water Resour. Res,* 2015.
16. Ekdale, A. A. and R. G. Bromley, Trace Fossils and Ichnofabric in the Kjolby Gaard Marl, Uppermost Createaceous, Denmark. Bull Geol. Soc. Denmark, 1993. **31**: p. 107–119.
17. Tie, H., OIL RECOVERY BY SPONTANEOUS IMBIBITION AND VISCOUS DISPLACEMENT FROM MIXED-WET CARBONATES, in Department of Chemical and Petroleum Engineering. 2006, The University of Wyoming: Laramie, Wyoming. p. 238.
18. Schutjens, P. M. T. M., et al. THE INFLUENCE OF INTERGRANULAR MICROCRACKS ON THE PETRO-PHYSICAL PROPERTIES OF SANDSTONE-EXPERIMENTS TO QANTIFY EFFECTS OF CORE DAMAGE. in *International Symposium of the Society of Core Analysts*. 1995. San Francisco, CA.
19. Klein, E. and T. Reuschle, A Model for the Mechanical Behaviour of Bentheim Sandstone. *Pure applied Geophysics,* 2003. **160**: p. 833–849.
20. Fack, F., et al., Bevacizumab treatment induces metabolic adaption toward anaerobic metabolism in glioblastomas. *Acta Neuropathologica,* 2015(129): p. 115–131.
21. Haldorsen, I. S., et al., Multimodal Imaging of Orthopic Mouse Model of Endometrial Carcinoma. *PLoS ONE,* 2015. **10**(8): p. e0135220.
22. Haugen, A., M. A. Fernø, and A. Graue. Numerical simulation and sensitivity analysis of in-situ fluid flow in MRI laboratory waterfloods offractured carbonate rocks at different wettabilities. in *SPEATCE*. 2008. Denver, CO, USA.